The wide field monitor and spectrometer instrument on board the ASTENA satellite mission concept

Fuschino, F., Campana, R., Caroli, E., Amati, L., De Cesare, G., et al.

F. Fuschino, R. Campana, E. Caroli, L. Amati, G. De Cesare, C. Labanti, M. Orlandini, E. Virgili, P. Rosati, F. Frontera, "The wide field monitor and spectrometer instrument on board the ASTENA satellite mission concept," Proc. SPIE 10699, Space Telescopes and Instrumentation 2018: Ultraviolet to Gamma Ray, 106995Z (14 September 2018); doi: 10.1117/12.2314473

SPIE.

Event: SPIE Astronomical Telescopes + Instrumentation, 2018, Austin, Texas, United States

The Wide Field Monitor and Spectrometer Instrument on board the ASTENA satellite mission concept

F. Fuschino[1], R. Campana[1], E. Caroli[*1], L. Amati[1], G. De Cesare[1], C. Labanti[1], M. Orlandini[1]
E. Virgilli[2], P. Rosati[2], F. Frontera[2]
[1]INAF/OAS of Bologna (Italy), Via Gobetti 101, I-40129 Bologna, Italy; [2]University of Ferrara, Dept. of Physics and Earth Science, Via Saragat 1, I-44122 Ferrara, Italy

ABSTRACT

The ASTENA mission concept under study in the framework of the H2020 AHEAD project includes a wide field monitor and spectrometer (WFM/S), mainly dedicated to GRBs. The instrument, composed by different units, is sensitive in the range 1 keV – 20 MeV. The total isotropic detection area will be ~3.0 m2 with a FOV of about 1.35 sr. The WFM will allow the detection and spectroscopic and polarimetric characterization of all classes of GRBs. Each module is a coded mask telescope that will allow the source localization within few arcmin up to 50–100 keV. The detector core is based on the coupling of low-noise, solid-state Silicon Drift Detectors (SDDs) with CsI(Tl) scintillator bars. Low-energy and high-energy photons are discriminated using the on-board electronics. The instrument design and preliminary experimental characterizations are reported and discussed.

1. INTRODUCTION

Gamma-Ray Bursts (GRBs) are one of the most challenging phenomena in modern space sciences. These phenomena are characterized by both huge luminosities up to more than 1000 erg/s and very wide redshift distribution extending from very low z (~0.01) up to z > 9, and are associated with peculiar core-collapse supernovae and with neutron star/black-hole mergers. Therefore, their study is of very high interest for several fields of astrophysics. These include, e.g., the physics of matter in extreme conditions and plasma physics, black hole physics, core-collapse SNe, cosmology and fundamental physics as the production of gravitational wave signals. Despite the huge observational advances occurred in the last twenty years, several open issues still affect our comprehension of these phenomena, and their exploitation for the solution of fundamental physics and cosmological problems. [1–3]

Among the most relevant aspects are all those connected with the so-called "prompt" emission. A better knowledge of both the emission processes and the source geometry is required, to clarify the origin of the "central engine" and its connection with the progenitors, and, furthermore, to assess the real energy budget involved in different classes of GRBs to use the GRBs observations for fundamental physics and cosmology studies. To address these fundamental issues, time resolved spectroscopy and possibly polarimetry of the GRB prompt emission over a broad energy range from few keV to up to several MeVs are mandatory requirements for next generation of hard X and soft γ-ray space instruments.

In this perspective, the ASTENA mission concept [4] under study in the framework of the H2020 AHEAD project includes a wide field monitor and spectrometer (WFM/S), mainly dedicated to GRB science. The instrument is sensitive in the range 1 keV – 20 MeV and is composed of several independent detection units, having a total isotropic detection (i.e. exposed) area up to ~3.0 m^2 over a FOV larger than 1 sr. The WFM/S will allow the detection and both spectroscopic and polarimetric characterization of all classes of GRBs and other high-energy transients. Each module is a coded mask telescope that will allow the source localization within few arcmin up to above 50 keV. The detector core is based on the coupling of low-noise, solid-state Silicon Drift Detectors (SDDs) with CsI(Tl) scintillator bars, and low energy and high-energy photons are discriminated using the on-board electronics.

[*]ezio.caroli@inaf.it; Phone: +390516398678

Space Telescopes and Instrumentation 2018: Ultraviolet to Gamma Ray, edited by Jan-Willem A. den Herder, Shouleh Nikzad, Kazuhiro Nakazawa, Proc. of SPIE Vol. 10699, 106995Z · © 2018 SPIE
CCC code: 0277-786X/18/$18 · doi: 10.1117/12.2314473

2. THE WFM/S INSTRUMENTS

The heritage of the ASTENA WFM/S instruments belong to a design studied in the framework of the THESEUS ESA M5 proposal [5].

2.1 WFM/S Main Characteristics

The WFM/S comprises six blocks of three identical coded mask telescope units, called *modules*. In each block, the modules are pointed at offset directions in such a way that their FOVs partially overlap. Each module has imaging capabilities in the low energy band (2 to ~50 keV) thanks to the presence of a coded mask placed above a position-sensitive detector. In the baseline configuration, the footprint of each WFM/S module is ~50×50×85 cm^3, with a total mass of about 37 kg, requiring a power budget of about 30 W.

Because of their configuration (Table 1), inside this energy band each module has an angular resolution of few arcmin over a partially coded field of view (FWHM) of ~0.5 sr. A passive shield around the mechanical structure between the mask and the detector plane, as well as limiting the cosmic ray diffuse background in the low-energy band, will determine the FOV of each module for X-rays up to about 150 keV. Above this energy and up to ~20 MeV the WFM/S module has almost isotropic detection capabilities. WFM/S modules and the other instrument on-board ASTENA, the Laue-lens based telescope NFT, are partially coaxial, in order to guarantees that the NFT field of view is centred in the overall WFM/S FOV. Furthermore, ASTENA WFM/S can operate also as a scattering polarimeter, due to 3D imaging capability of the module detector planes.

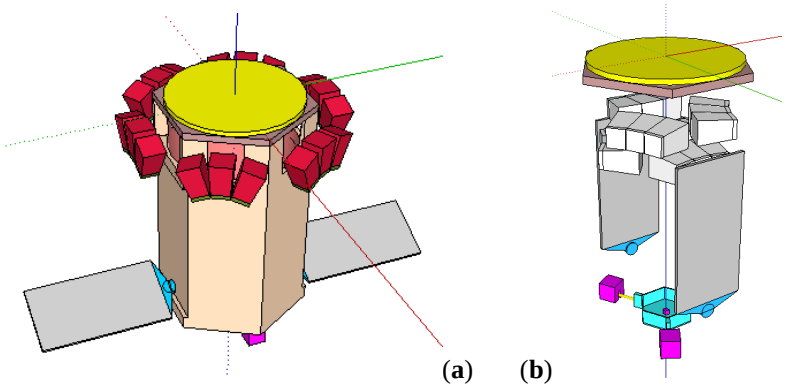

Figure 1. (a) The WFM/S instrument (red volumes) on board the ASTENA satellite in deployed configuration; (b) The WFM/S instrument in launch configuration.

2.2 WFM/S GRB's sensitivity

Using a reference background in a LEO orbit, Figure 2 shows the expected sensitivity of the ASTENA WFM/S in different energy bands as function of the GRB duration in seconds. This preliminary evaluation shows a sensitivity already at least an order of magnitude better with respect to currently proposed instrumentation (e.g. THESEUS) dedicated to GRB science.

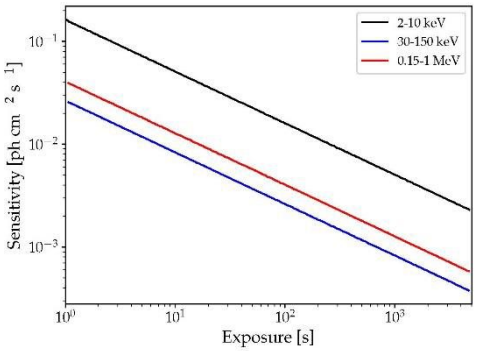

Figure 2: The ASTENA WFM/S evaluated 3σ sensitivity to GRB's as function of the measure time (exposure) in different energy band.

3. THE WFM/S SUBSYSTEMS

As stated before, the ASTENA WFM/S module is a heritage the THESEUS mission study. In the following sections, we provide a short description of both the main characteristic of each ASTENA WFM/S subsystems.

3.1 WFM/S Single coded mask telescope

The basic module of the WFM/S is a coded mask telescope that can provide imaging up to ~50 keV in the current design inherited by the ESA M5 THESEUS proposal. In the ASTENA mission study, we will verify the opportunity and feasibility to extend this imaging capability up to 100 keV, minimizing the impact in the system complexity and resources requirements. The masks of each telescope will be designed individually, to minimize direction reconstruction ambiguities, and will be built with self-supporting random patterns to be optimized by using Monte Carlo simulations.

Each WFM/S coded mask telescope have a passive shield (hopper) connecting the mask to the detector plane, made by graded layers of different materials to optimize the opacity up to 150 keV, limiting the cosmic X-ray background contribution on the detector. Furthermore, the hopper, limiting the telescope FOV up to 150 keV, would allow a rough location capability (several degrees) by comparing the detected counts over all the mask telescope units (see following subsections).

Table 1. Main baseline characteristics of the ASTENA WFM/S coded mask telescope module

Mask Pattern	Random self-supporting
Element size	5×5 mm^2
Open fraction	30-50%
Dimension	50 cm × 50 cm
Mask-Detector Dist.	70 cm
Mask Material	Steel
Mask Thickness	0.5-1 mm
Hopper Material	W/Cu/Mo
Hopper thickness	1-1.5 mm

3.2 WFM/S Block Unit

In the current ASTENA configuration shown in Figure 1, the coded mask telescope modules are arranged in block units, placed around the NFT Laue lens instrument. Three coded mask telescope modules make each WFM/S block unit. The optical axis of the coded mask modules in the block unit are not coaxial, but the relative inclination (offset) between the optical axis of each coded mask module is optimized to maximize total FOV of the WFM/S, taking into account also the satellite bus constraints.

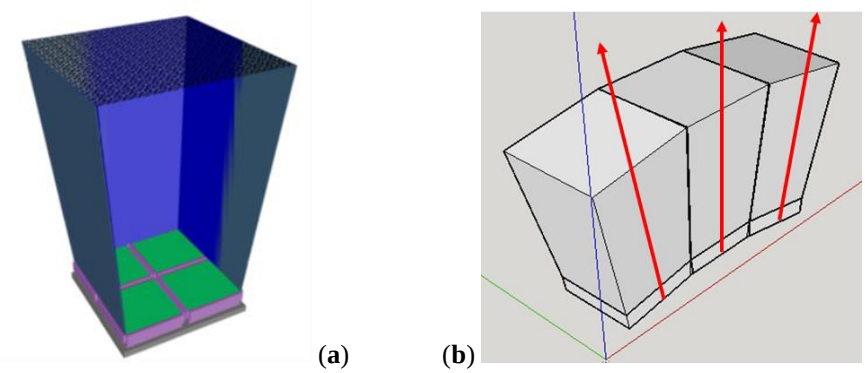

(**a**) (**b**)

Figure 3. (a) The coded mask telescope module scheme that is the basic element of the ASTENA WFM/S in which are clearly visible the random mask on the top, the detection plane in the form of a 2x2 mosaic of CsI/SDD sensitive element arrays, and in between the hopper shield. (b) The schematic drawn of the block unit made by three coded mask modules. The red arrows show the optical axis of each module with their non-parallel directions.

3.3 WFM/S Block Field of View

Assuming ±20° as the reciprocal offset of the optical axis of each module in the block unit, the WFM/S Block unit FOV at 100 has been analytically evaluated and it is shown in Figure 4. The contour plot, left, shows the FOV as function of the exposed detector area percentage, while the plot on the right reports the angular profile of the response of each module hopper. The overall angular response of the block unit is the convolution of the single module response profile and is given by the superimposed red thick line.

Since the current ASTENA implementation foresees 6-block unit distributed along the perimeter of a hexagonally shaped service module (one for each hexagon side), the overall FOV of the WFM/S is obtained by the superimposition of the single block FOV with each major axis rotated by 60°. The total FOV (FWHM) is ~1.35 sr, with a total exposed area of ~3000 cm^2.

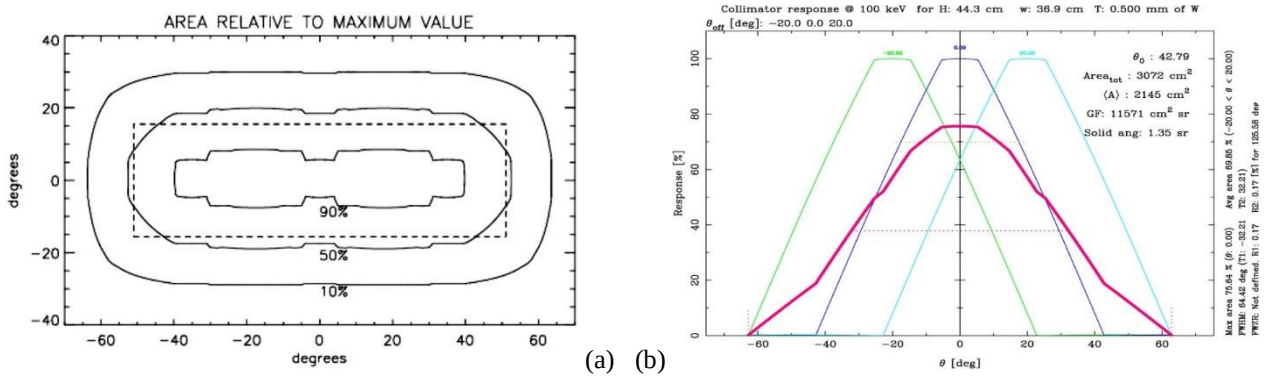

(a) (b)

Figure 4. (a) The shape and the angular dimension of the ASTENA WFM/S block unit at 100 keV. Each contour line represent the FOV for corresponding to a given sensitive area exposure. (b) The profile of the hopper (or collimator) response versus the seeing angle of each coded mask module in a block unit. In red the overall angular profile response of the single WFM/S block unit.

3.4 WFM/S Mask Telescope Detector

A 2×2 mosaic of segmented detector modules constitutes the coded mask detector plane. Each detector module is an array of CsI(Tl) bars, each read out by two Silicon Drift Detectors (SDD) cells, placed at the two bar ends (Figure 5a). In turn, each array consists of basic sensitive units composed by 2×2 CsI(Tl)+SDD elements [6]. The current design foresees the use of SDD cells with a sensitive area of 5×5 mm2 optically coupled with CsI(Tl) bars with the same cross-section and a length between 3 to 5 cm.

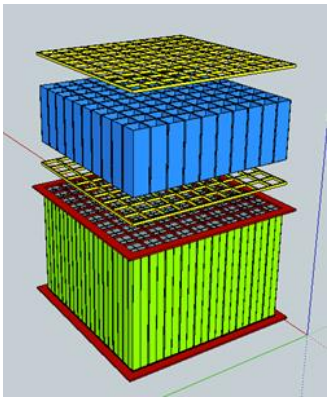

(a)

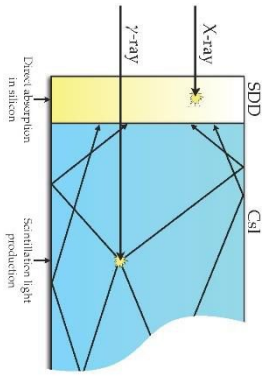

(b)

Figure 5. (a) The exploded view of the detector module: the yellow grids represent the support of the SDD that are optically coupled to the extremes of the CsI bars (blue array), the segmented green volume represent the associated front-end electronics. (b) The *siswich* read-out concept. Low energy X-ray (<50 keV) are detected in the top SDD, while the hard X/soft γ-rays (20 keV to 20 MeV) interact with higher probability inside the CsI bar generating optical photons that are readout by the two SDD coupled at each extreme.

Aiming at designing a compact instrument with a very wide sensitivity band, the detector module is based on the so-called *siswich* concept [7], exploiting the optical coupling of Silicon detectors with inorganic scintillator bars. As shown by the schematic in Figure 5b, the topmost SDD array acts as a low energy detector (LED), while the scintillator bar detector operates as a high energy detector (HED) with 3D spatial resolution capabilities. In this concept, the top SDD play the double role of read-out devices for the signal from the scintillator and of an independent low energy solid state X-ray detector.

The two types of events are distinguished by techniques based on pulse shape discrimination, through the different rise times of the corresponding preamplifier signal. In the case of low energy X ray events interacting in the SDD, the rise time is dominated by the anode collection time (~100 ns). For higher energy photons, interacting in the CsI(Tl) scintillator, the signal rises following the convolution of the characteristic CsI(Tl) scintillation de-excitation time constants and different light paths, amounting to an effective rise time of a few μs.

Table 2. The detector module main characteristics

Energy band	2 keV – 20 MeV
Module mosaic	2×2
Pixels/module	32×32
Sensitive area	256 cm^2
Pixel size/shape	5 mm/Square or Hexagonal
LED (2-50 keV)	SDD 450 μm thick
HED (20 keV-20 MeV)	CsI(Tl) 3 to 5 cm thick

4. THE WFM/S DETECTOR PERFORMANCE

In order to demonstrate the validity of the proposed instrument architecture for the detector plane, a prototype is under development and it is currently in its characterization phase. The obtained experimental results have confirmed the feasibility and the expected performance of the proposed detector concept. In the following sections, we will give a summary of the achieved results.

4.1 Spectroscopic Response of the Silicon Drift Detector units

The SDD are used for both soft X-ray detector and as CsI(Tl)-scintillator readout. This capability is well evident from Figure 6, where two simultaneous spectra acquired by the top SDD with two radioactive sources are reported. Event generated by the ^{241}Am source emission is directly detected by the SDD (black line), while the higher-energy ^{137}Cs spectrum is the results of the SDD readout of the scintillating photons generated inside the CsI(Tl) bar unit (blue line). Both types of events were acquired at the preamplifier output simultaneously by a fast digitizer (60 MS/s) and then

distinguished with algorithms for pulse shape discrimination on the rising edge, and finally optimized digital filters were applied separately for the two categories of events.

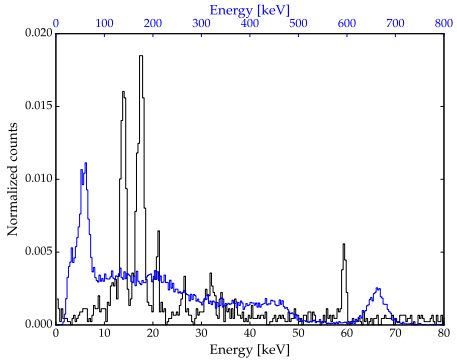

Figure 6. Simultaneous acquisition of a ^{137}Cs plus a ^{241}Am source by SDD. The black curve (lower x-axis) is the spectrum of ^{241}Am photon detected by the SDD, while the blue one (upper x-axis) is the spectrum of ^{137}Cs events detected in the CsI bar unit and readout by the top SDD through the generated scintillation photons.

The good performance of the digital signal processing methods are thus demonstrated, showing a comparable result with respect to a more traditional acquisition chain composed by an analogue shaping amplifier coupled to a commercial multichannel analyser. The setup shows a very good spectral resolution of ~5% (FWHM) at 662 keV for scintillation events, and a ~300 eV (rms) resolution at 6 keV for X-ray events at temperature of -30 °C.

4.2 Spatial resolution response of the CsI sensitive elements.

Each CsI(Tl) sensitive element has the lateral surfaces wrapped by a highly diffusive material able to provide an exponential decay with the distance of the scintillation cloud generation point along the of the major axis. This method was implemented for the first time in early 80's in the NaI detection plane ZEBRA balloon borne coded mask telescope [8] and in more recent years on the mini-calorimeter of the AGILE satellite payload [9]. The scintillation light that reach the SDD devices at the two extreme of the CsI(Tl) bar is then described by:

$$N_A = N_0 e^{-\alpha\left(\frac{L}{2}-x\right)}; \quad N_A = N_0 e^{-\beta\left(\frac{L}{2}+x\right)} \tag{1}$$

where N_0 is the number of the scintillation photons generated at the interaction point along the CsI(Tl) bar (x), N_A and N_B represent the number of the scintillation photons reaching the left and the right, respectively, end of each CsI(Tl) bar, L is the CsI(Tl) bar length. The parameter N_0 depends on the energy (E_γ) deposited in the CsI(Tl) elements. Finally, α and β are the measured attenuation coefficients in the two opposite scintillation light travelling directions as the result of the CsI(Tl) diffusive wrapping. In the equation (1), the origin of the major axis is set at $x=L/2$. Using the knowledge of the attenuation coefficient and the signals collected at the two ends given by equation (1) is then possible to reconstruct the X/γ photon interaction position along the CsI(Tl) element major axis by means of the following relation:

$$\langle x \rangle = \frac{\ln\left(\frac{N_B}{N_A}\right) - \frac{L}{2}(\beta - \alpha)}{\alpha + \beta} \tag{2}$$

where $\langle x \rangle$ is the estimated position along the CsI bar major axis.

Figure 7a gives an example of the signal amplitude readout by the SSD device at each end of a CsI(Tl) bar with a length of 50 mm using the 662 keV photons from a ^{137}Cs source. From these measurements, it is possible to evaluate for each CsI(Tl) sensitive elements the characteristic attenuation coefficient α and β. The solid lines are the linear best fits of the measured signals as function of the source position along the CsI(Tl) bar major axis. These best fits give for the scintillation light attenuation coefficients α and β the values (in mm^{-1}) of 0.0248 ± 0.0004 and 0.0245 ± 0.0010, respectively. Figure 7b show the reconstructed position of 662 keV photons from a collimated ^{137}Cs source. The average FWHM of the

reconstructed position is ~3 mm. Considering the source spot size in these measurements (~2 mm), the derived intrinsic resolution in position for the γ ray interaction is around 2.2 mm (FWHM)..

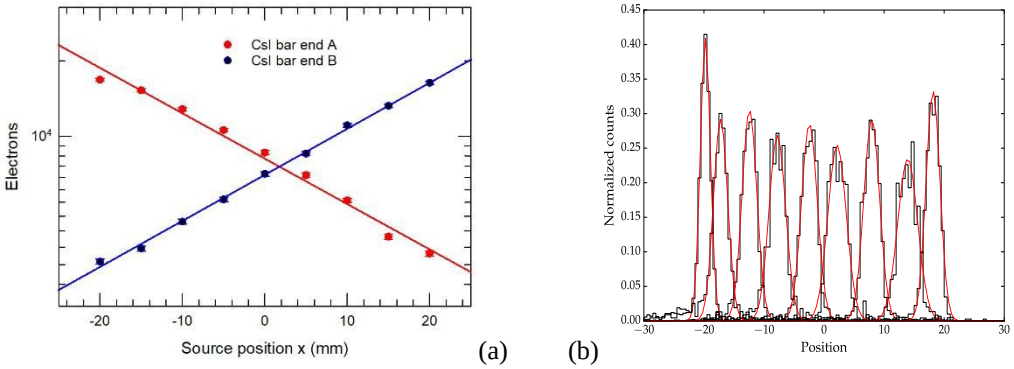

(a) (b)

Figure 7. (a) Measurements of the signal readout by SDD device at the two CsI bar ends showing the linear attenuation of the signal logarithm with the source location along the bar major axis. The circle are the measured signal intensities in electrons, while the solid lines represents the linear best fits. (b) The reconstructed position along the CsI bar major axis. The resolution (FWHM) is ~ 2 mm over 50 mm.

4.3 CsI response model for spectral resolution

The energy of each photons interacting inside the CsI(Tl) sensitive elements can be evaluated by the product of the signals readout by the SDD device at the two opposite ends. Using the expression in equation (1) for the two signals, we can easily derive the relation to calculate the energy deposited in a given position along the CsI(Tl) bar major axis:

$$\langle E_\gamma \rangle = k\langle N_0 \rangle = k\sqrt{N_A \cdot N_B} \cdot e^{\frac{L}{4}(\alpha+\beta)} \cdot e^{\frac{x}{2}(\alpha-\beta)} \tag{3}$$

Equation (3) show that the reconstructed energy, corresponding to the same deposited energy, is not constant along the CsI(Tl) bar major axis. This dependence is the results of the non-symmetrical behaviour of the scintillation light attenuation across the CsI(Tl) element toward the two opposite ends: i.e. the attenuation coefficients α and β are slightly different. In fact, this demonstrates the importance of minimizing this difference by optimizing both the diffusion wrapping process on the individual CsI(Tl) elements and their optical coupling with the SDD reading devices.

Figure 8a shows the spectrum obtained with a collimated ^{137}Cs source at the bar centre. The measured resolution at 662 keV is 4.9% (FWHM), with a lower threshold of about 20 keV, thus confirming the expected results and the good performance of the system. Figure 8b plots the reconstructed energy of the 662 keV peak of same radioactive source along the CsI(Tl) bar major axis. The two pink short dashed lines give the ±1σ region, that is ~20 keV wide. A results that is again compatible with the with the low energy threshold of the CsI(Tl)/SDD system.

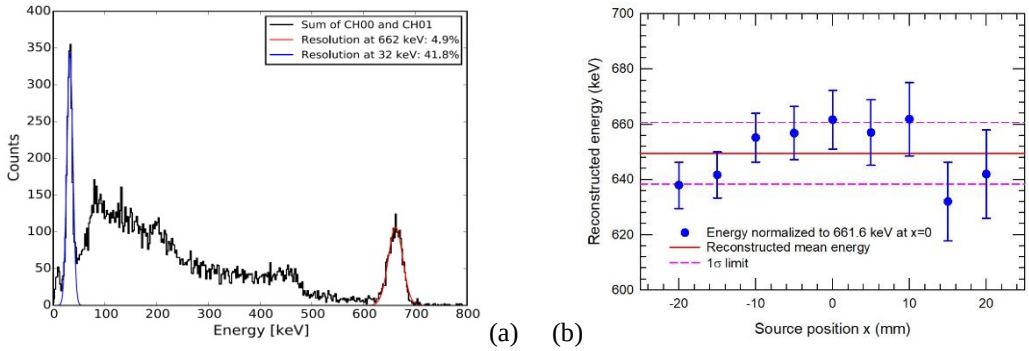

(a) (b)

Figure 8. (a) A spectrum obtained with the ^{137}Cs source at the bar centre is shown. The measured resolution at 662 keV is 4.9%, with a lower threshold of ~20 keV, thus confirming the expected results and the good performance of the overall system. (b) The normalized reconstructed energy along the major CsI bar axis obtained using the attenuation coefficient evaluated by data reported in Figure7a. The short dashed pink lines give the ± 1σ spread.

4.4 WFM/S GEANT 4 Simulation Results

In order to evaluate the scientific performance of the ASTENA WFM/S in detecting and positioning GRB events, a Monte Carlo model has been developed using the Geant-4 framework to aid the feasibility study of the THESEUS XGIS detector. The mass model and the simulator are now being updated to fit the design foreseen for the ASTENA mission.

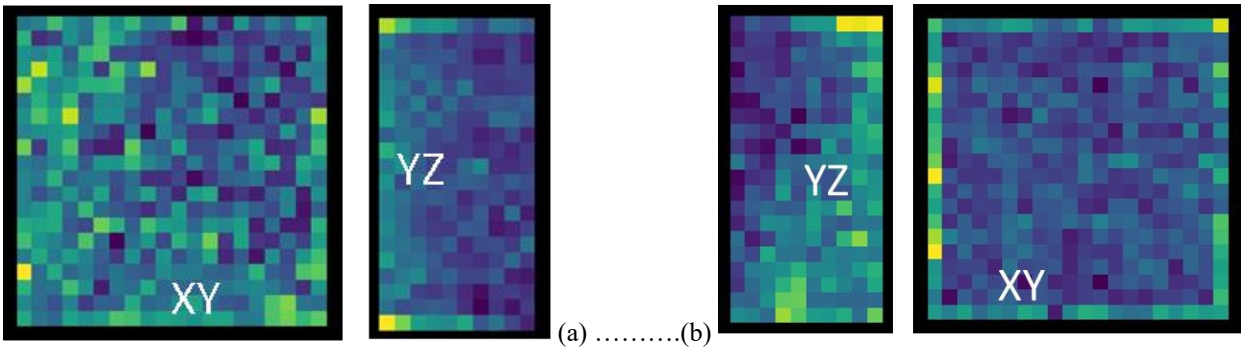

Figure 9. False colour maps of the counts detected by a CsI coded mask module illuminated by a parallel flux at 1 MeV with two different incoming directions, both external to Mask FOV: (a) (θ,ϕ)=(40°, 0°) (b) (θ,ϕ)=(70°, 210°), where θ is the zenithal angle and ϕ the azimuthal angle of the impinging flux.

As an example of the results, the reconstructed spatial distribution of CsI(Tl) events obtained with a WFM/S module is shown in Figure 9. In this particular case, the reconstructed events in each CsI(Tl) bar is discretized along the main axis in 10 segments 5 mm wide (i.e., twice the measured 1σ spatial resolution). Therefore, the coded mask module CsI(Tl) detector is equivalent to a 3D detector with voxels of 5×5×5 mm3. This characteristic is particularly interesting, because it opens the possibility to use the detector also as a Compton detector, and in particular as a Compton scattering polarimeter.

From the distribution of the detected counts and the capability to reconstruct the photon incoming direction by Compton cinematics over all WFM/S modules is possible to infer the GRB incoming direction within an angular precision that depends on its fluency, energetic and position.

5. CONCLUSIONS

A sensitive and broad-band X and γ-ray instrument is needed to fulfill the ASTENA main scientific objectives that is to reliably identify and accurately positioning (at better than one arcmin) GRBs to allow fast high energy follow up measurement with the high sensitivity broadband Laue lens telescope (NFT). The proposed ASTENA WFM/S monitor design will allow also measuring high-energy transients on short timescales with contemporary good spectroscopic and polarimetric capabilities, allowing detailed investigation of the energetic and temporal evolution of these sources.

Of course, several trade-offs and improvements on the basic design outlined in this paper can be foreseen. The field of view of a single unit, the coded mask open fraction (and its impact on efficiency and sensitivity), but also the choice of scintillator thickness, geometry and type (and its impact on efficiency and spectral resolution), besides the detailed triggering logic, should be optimized in a future assessment phase in order to maximize the ASTENA missions scientific returns.

REFERENCES

[1] Gehrels, N., and Meszaros, P., “Gamma-Ray Bursts”, Science , Vol. 337, N. 6097, p. 932 (2012)
[2] Kumar, P., and Zhang, B., “The physics of gamma-ray bursts & relativistic jets”, Physics Reports, Vol. 561, p. 1 (2015)
[3] Amati, L., and Della Valle, M., “Measuring Cosmological Parameters with Gamma Ray Burst”, Int. J. of Modern Physics D, Vol. 22, N. 14, id. 1330028 (2013)
[4] Rosati et al., “The Advanced Surveyor of Transient Events and Nuclear Astrophysics (ASTENA)”, Proposal of instrument concept in response to the Call issued by the H2020 AHEAD WP9 Instrument Working Group, https://drive.google.com/file/d/187vRVPB128lvVmjf2HAtnHbPJtcVYChM/view?usp=sharing (2016);
[5] Amati, L., et al. “The THESEUS space mission concept: science case, design and expected performances”, Advances in Space Research, Vol. 62, p. 191 (2018);

[6] Campana, R., et al, “A compact and modular x- and gamma-ray detector with a CsI scintillator and double-readout Silicon Drift Detectors”, Proc. of SPIE on Space Telescopes and Instrumentation 2016: Ultraviolet to Gamma Ray, Vol. 9905, p. 99056I (2016);
[7] Marisaldi, M., et al. "A Pulse Shape Discrimination Gamma-Ray Detector Based on a Silicon Drift Chamber Coupled to a CsI(Tl) Scintillator: Prospects for a 1 keV 1 MeV Monolithic Detector.", IEEE Transactions on Nuclear Science, Vol. 51: p. 1916 (2004);
[8] Charalamboulos, P.M., et al., “A two-dimensional low energy gamma-ray position sensitive detector”, Nucl. Instr. and Meth. in Phys. Res. A, Vol. 221, p. 184 (1984);
[9] Labanti, C., et al., "The minicalorimeter of the AGILE satellite," Proc. of SPIE on Space Telescopes and Instrumentation II: Ultraviolet to Gamma Ray, Vol. 6266, p. 62663Q (2006);